*Geophys. J. Int.* (1998) **132,** 1–13

# Shock-wave equation of state of rhyolite

William W. Anderson,* Wenbo Yang,† George Chen and Thomas J. Ahrens
*Lindhurst Laboratory of Experimental Geophysics, Seismological Laboratory, California Institute of Technology, Pasadena,* CA 91125, *USA.*
*E-mail: bill@gsw1500.gsw.peachnet.edu*

Accepted 1997 June 25. Received 1997 June 23; in original form 1997 February 10

## SUMMARY

We have obtained new shock-wave equation of state (EOS) and release adiabat data for rhyolite. These data are combined with those of Swegle (1989, 1990) to give an experimental Hugoniot which is described by $U_s = 2.53(\pm 0.08) + 3.393(\pm 0.37)u_p$ for $u_p < 0.48$ km s$^{-1}$, $U_s = 3.85(\pm 0.05) + 0.65(\pm 0.03)u_p$ for $0.48 \le u_p < 2.29$ km s$^{-1}$, $U_s = 1.52(\pm 0.08) + 1.67(\pm 0.02)u_p$ for $2.29 \le u_p < 4.37$ km s$^{-1}$, and $U_s = 3.40(\pm 034) + 1.24(\pm 0.06)u_p$ for $u_p \ge 4.37$ km s$^{-1}$, with $\rho_0 = 2.357 \pm 0.052$ Mg m$^{-3}$. We suggest that the Hugoniot data give evidence of three distinct phases—both low- and high-pressure solid phases and, possibly, a dense molten phase. EOS parameters for these phases are $\rho_0 = 2.494 \pm 0.002$ Mg m$^{-3}$, $K_{S0} = 37 \pm 2$ GPa, $K' = 6.27 \pm 0.25$, and $\gamma = 1.0(V/V_0)$ for the low-pressure solid phase; $\rho_0 = 3.834 \pm 0.080$ Mg m$^{-3}$, $K_{S0} = 128 \pm 20$ GPa, $K' = 3.7 \pm 1.4$, and $\gamma = 1.5 \pm 0.5$ for the solid high-pressure phase; and $\rho_0 = 3.71 \pm 0.10$ Mg m$^{-3}$, $K_{S0} = 127 \pm 25$ GPa, $K' = 2.1 \pm 1.0$, and $\gamma = 1.5 \pm 1.0$ for the dense liquid. Transition regions of the Hugoniot cover the ranges of 9–34 GPa for the low-pressure–high-pressure solid transition and 90–120 GPa for the high-pressure solid–liquid transition. Release paths from high-pressure states, calculated from the EOS parameters, suggest that the material remains in the high-pressure solid phase upon release. Release paths from both the high-pressure solid and liquid fall above the Hugoniot until the Hugoniot enters the low-pressure–high-pressure mixed phase region, when the release paths then cross the Hugoniot and fall below it, ending at significantly higher zero-pressure densities than that of the low-pressure phase. The low-pressure release paths fall very close to the Hugoniot. Estimates of residual heat deposition, based on shock-release path hysteresis, range from 20 to 60 per cent of the shock Hugoniot energy.

**Key words:** equations of state, rhyolite, shock waves.

## INTRODUCTION

Granite is the primary component of upper continental crust, and rhyolite, its extrusive equivalent, is a common near-surface material in many areas of continental crust. Granite is composed primarily of quartz and feldspars and has a shock Hugoniot curve very similar to the Hugoniots of these minerals (Sekine *et al.* 1995). Rhyolite, while chemically similar, is mineralogically distinct from granite in that it contains a large proportion of either glass or hydrous alteration products. In either case, rhyolite is usually significantly less dense than granite and can have abundant void space which is often water-filled *in situ*. These considerations suggest that the shock-wave behaviour of rhyolite may not be reliably modelled using data derived from granite.

At very high pressures, where the phases tend to be in closest-packed configurations, differences between the Hugoniots of granite and rhyolite will be minor and due primarily to differences in initial density. This also implies that the high-pressure region of the rhyolite Hugoniot can be modelled by mixing the high-pressure equivalents of the relevant silicate minerals or elemental oxides. At lower pressures, however, the differences between rhyolite and granite require that both materials be studied independently.

The purpose of this study is to present new experimental data for shocked and partially released states of rhyolite and to combine these with previous data to obtain a complete equation of state (EOS). We also consider the implications of porosity for shock propagation, especially in relation to variation between the Hugoniot curves of water-saturated versus dry rhyolite.

* Now at: Department of Geology and Physics, Georgia Southwestern State University, 800 Wheatley Street, Americus, GA 31709, USA.
† Now at: Perforating and Testing Center, Schlumberger, Inc., PO Box 1590, Rosharon, TX 77583, USA.

## PREVIOUS WORK

Previously, Swegle (1989, 1990) reported Hugoniot and release adiabat data for rhyolite, whereas Marsh (1980) presented Hugoniot data for both dry and water-saturated rhyolitic tuffs. Trunin *et al.* (1988) obtained a Hugoniot for a very dense tuff. Swegle obtained EOS parameters for use in calculating Hugoniot and release adiabat states for both the high-pressure 'phase' and the low-pressure 'phase' of rhyolite. He suggested that the high-pressure phase properties of rhyolite should be similar to those of stishovite and presented a comparison of shock wave data for $SiO_2$ and rhyolite that supports this assumption.

## EXPERIMENTAL PROGRAMME

### Samples

The samples used for this study are a zeolitized rhyolite from the Kearsage formation, Nye County, Nevada. The samples had a mean bulk density (including porosity) of $2.2939 \pm 0.0004$ Mg m$^{-3}$, determined by direct measurement of the mass and volume calculated from linear dimensions. The mean Archimedian density, determined by weighing dry and suspended in toluene, is $2.4929 \pm 0.0005$ Mg m$^{-3}$. In both cases, the stated uncertainties represent one standard deviation in the measured values. The whole-rock physical properties of the rhyolite are summarized in Table 1. Table 2 gives compositional information, which was provided with the present samples. Because rhyolite is very fine grained, mineralogical data cannot be easily obtained using standard microscopic point-counting techniques. Instead, we report the calculated CIPW normative mineral assemblage (Kelsey 1965) in Table 3. The CIPW norm has several shortcomings, most notably that no provision is made for hydrous minerals such as micas. In the present case, the result is that there is an excess of $Al_2O_3$, which enters the norm as corundum. We have corrected this situation by combining the excess alumina with potassium feldspar to obtain an equivalent muscovite content (Table 3).

### Experiments

Shock waves in the samples were generated by impact of projectiles launched from the Caltech 25 mm two-stage light-gas gun and 40 mm propellant gun. The projectiles carried flat metal flyer plates which impacted driver plates upon which the samples were mounted. In each experiment the impact velocity of the projectile was measured by the flash X-ray method (Ahrens 1987), typically with an accuracy of ~0.5 per cent.

Most experiments were impedance match equation of state (EOS) experiments in which a rotating mirror or image converter streak camera was used to measure shock wave traveltime through samples of known thickness in order to determine the shock wave velocity. Flat and inclined mirrors placed against rear surfaces of the target (Fig. 1a) were employed to observe the shock wave arrival times to an accuracy of ~3 ns (Ahrens 1987). The Hugoniot state was determined by applying the impedance match conditions to the measured initial density, impact velocity and shock wave velocity. The Rankine–Hugoniot conservation relations are used to relate shock and particle velocity to density, pressure, specific volume and internal energy:

$$\rho_H = \rho_{00} \frac{U_s}{U_s - u_p}, \quad (1)$$

$$P_H = P_0 + \rho_{00} U_s u_p, \quad (2)$$

$$E_H = E_0 + \frac{1}{2}(P_H + P_0)(V_{00} - V_H) = E_0 + \frac{1}{2}u_p^2, \quad (3)$$

where $\rho$, $P$, $V$, and $E$ are mass density, pressure, specific volume and specific internal energy, respectively, and the subscripts '0' and 'H' refer to the initial and Hugoniot states, respectively. $U_s$ is the shock wave velocity and $u_p$ is the shock-induced particle velocity, both measured in the rest frame of the unshocked material. The subscript '00' assigned to $\rho$ and $V$ indicates the zero-pressure values of density or specific volume, including any initial porosity. $P_0$ is negligible compared to $P_H$ and is set to zero as is $E_0$, which is arbitrary.

A partially or fully released state along the release adiabat is also determined by a free-surface or buffer impedance mismatch measurement. These data are reduced by way of the

**Table 1.** Properties of Kearsage rhyolite used in the present experiments.

| | |
|---|---|
| Bulk Density | 2.2939±0.0004 Mg/m$^3$ |
| Crystal Density | 2.4929±0.0005 Mg/m$^3$ |
| $V_p$* | 3.652±0.051 km/s |
| $V_s$* | 2.309±0.031 km/s |
| $V_b$ | 2.512±0.085 km/s |
| $K_S$ | 15.73±1.06 GPa |
| Poisson's Ratio | 0.170±0.006 |

* Measured by ultrasonic pulse traveltimes.

**Table 2.** Composition of Kearsage rhyolite.*

| Oxide | Weight Percent |
|---|---|
| $SiO_2$ | 68.33 |
| $TiO_2$ | 0.30 |
| $Al_2O_3$ | 14.25 |
| FeO** | 1.93 |
| MnO | 0.06 |
| MgO | 0.27 |
| CaO | 1.02 |
| $Na_2O$ | 4.06 |
| $K_2O$ | 4.71 |
| $P_2O_5$ | 0.07 |
| $CO_2$ | 0.15 |
| $H_2O^+$ | 0.52 |
| $H_2O^-$ | 4.13 |
| Total | 99.80 |

* Analysis provided by US Geological Survey Core Library, Mercury, Nevada.
** Total Fe as FeO.

**Table 3.** Normative mineral composition of Kearsage rhyolite. Assumed $Fe_2O_3/FeO$ molar ratio is 0.43.

| Mineral/Component | CIPW Norm (Weight %) | Corrected Norm (Weight %) |
|---|---|---|
| Quartz | 24.02 | 24.02 |
| Corundum | 1.13 | --- |
| Orthoclase | 27.83 | 24.75 |
| Albite | 34.35 | 34.35 |
| Anorthite | 3.65 | 3.65 |
| Hypersthene | 2.20 | 2.20 |
| Magnetite | 1.44 | 1.44 |
| Ilmenite | 0.57 | 0.57 |
| Apatite | 0.16 | 0.16 |
| Calcite | 0.34 | 0.34 |
| Muscovite* | --- | 4.41 |
| "Water"* | --- | 4.13 |
| Total | 95.69 | 100.02 |

* Not used in CIPW norm.

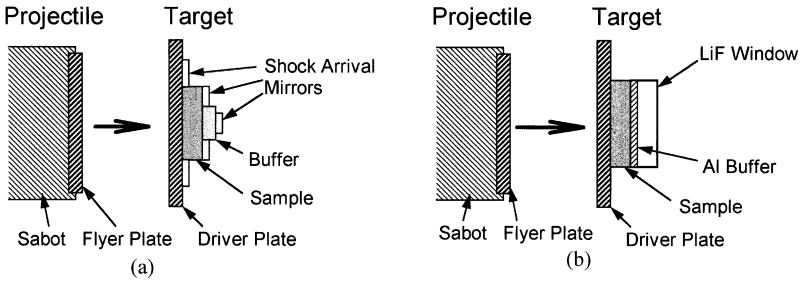


**Figure 1.** Schematic of experiments. (a) EOS experiment with buffer. Shock states are determined by impedance matching. (b) VISAR. Shock particle velocity profiles at the buffer–window interface are modelled by 1-D hydrocodes to determine stress–strain history in sample.

Riemann integral formalism (Rice, McQueen & Walsh 1958; Lyzenga, Ahrens & Mitchell 1983). Lexan plates and polystyrene foam pads mounted at the rear of the samples were used as buffer materials.

Several experiments employed a velocity-sensitive interferometer (VISAR, Barker & Hollenbach 1972) to investigate compressive and release wave profiles in the range 6–31 GPa (Yang *et al.* 1994). This technique makes use of the Doppler shift of reflected laser light produced by a modified Michelson interferometer and recorded using photomultiplier tubes and digitizing oscilloscopes. The VISAR used in the present experiments incorporates a push–pull modification (Hemsing 1979) for improved signal quality. The time resolution of our VISAR is $\sim 3$ ns, with a velocity precision of $\sim 1$ per cent. The target assembly for these experiments (Fig. 1b) consisted of an aluminum driver plate, a rhyolite target, a diffusely reflecting aluminum buffer and a LiF window. For one shot, the flyer plate was rhyolite and it impacted the aluminum buffer directly. For some of the VISAR experiments, Hugoniot data were also obtained from the records of shorting pin signals and the VISAR signal, although such results are less reliable than those from the impedance matching experiments.

## Experimental results

The experimental results are given in Table 4. The $U_s$–$u_p$ and $P$–$V$ projections of these data are shown in Figs 2 and 3, along with the data from Swegle (1989, 1990). Release adiabat paths from the impedance matching data are obtained using the straight-line approximation of Lyzenga & Ahrens (1978). The VISAR release paths are calculated using the WONDY 1-D finite difference hydrocode (Kipp & Lawrence 1982) to be consistent with the observed velocity–time profile. Often, $U_s$ is represented as a polynomial function of $u_p$:

$$U_s = C_0 + su_p + s'u_p^2 + \ldots . \quad (4)$$

The present data can be modelled as a series of four linear segments in the $U_s$–$u_p$ plane. The parameters describing these segments are presented in Table 5. Unfortunately, the number of segments relative to the number of data results in the fit parameters describing each segment having relatively large uncertainties. However, the rhyolite studied by Swegle (1989, 1990) is sufficiently similar to that used in the present study that we can combine the two data sets to provide much tighter constraints on the $U_s$–$u_p$ Hugoniot. The average initial density of samples in the combined data set, with a one-standard-deviation uncertainty, is $\rho_{00} = 2.357 \pm 0.052$ Mg m$^{-3}$, corresponding to a porosity of $\sim 5.5$ per cent for the same value of $\rho_0$. The Hugoniot curve still displays the same segments (Fig. 2), but the parameters describing those segments, which are also listed in Table 5, are now much more tightly constrained.

The elastic wave observed in experiment 894 has a pressure of $2.76 \pm 0.34$ GPa and a velocity of $4.55 \pm 0.11$ km s$^{-1}$. We

**Table 4.** Experimental data for Kearsage rhyolite.

| Shot | Flyer/ Driver | Impact Velocity (km/s) | Sample Density ($Mg/m^3$) | Shock State | | | | Release State | | |
|---|---|---|---|---|---|---|---|---|---|---|
| | | | | Particle Velocity (km/s) | Shock Velocity (km/s) | Pressure (GPa) | Density ($Mg/m^3$) | Particle Velocity (km/s) | Pressure (GPa) | Density ($Mg/m^3$) |
| 894 | Al2024 | 1.011 (.002) | 2.288 (.002) | .265[a] (.032) .648[b,c] (.028) | 4.551[a] (.114) 3.697[b,c] (.652) | 2.76[a] (.34) 5.95[b,c] (.49) | 2.429[a] (.019) 2.735[b,c] (.001) | 1.385[d] (.212) | 0[d] | 2.190[d] (.192) |
| 887 | Al2024 | 1.06 | 2.29 | | | 6.27[h] | 2.741[h] | | (VISAR) | |
| 886 | Al2024 | 1.45 | 2.298 | | | 9.08[h] | 2.908[h] | | (VISAR) | |
| 888 | Al2024 | 1.970 (.010) | 2.291 (.007) | 1.245 (.009) | 4.456 (.059) | 12.71[i] (.14) | 3.180[i] (.024) | | (VISAR)[i] | |
| 890 | W | 1.956 (.007) | 2.2775 (.0010) | 1.718 (.005) | 5.014 (.114) | 19.62 (.39) | 3.465 (.044) | 2.035[e] (.178) 3.242[d] (.216) | 13.35[e] (1.85) 0[d] | 3.283[e] (.406) 2.417[d] (.316) |
| 892 | Ta | 2.364 (.017) | 2.261 (.002) | 2.006 (.011) | 4.929 (.090) | 22.36 (.37) | 3.813 (.054) | 2.230[e] (.143) | 15.41[e] (1.57) | 3.711[e] (.275) |
| 893 | Ta | 2.359 (.006) | 2.280 (.003) | 1.991 (.011) | 5.093 (.090) | 23.12 (.37) | 3.744 (.049) | 2.308[e] (.031) | 16.27[e] (.24) | 3.548[e] (.086) |
| 930 | W | 2.292 (.011) | 2.292 (.002) | 2.011 (.011) | 5.093 (.100) | 23.47 (.43) | 3.787 (.054) | 2.500[e,g] (.255) 3.238[f,g] (.091) | 18.47[e,g] (3.13) 0.59[f,g] (.06) | 3.207[e,g] (1.423) 2.921[f,g] (1.149) |
| 929 | W | 2.500 (.010) | 2.301 (.002) | 2.190 (.009) | 5.197 (.055) | 26.18 (.27) | 3.976 (.035) | 2.517[e] (.131) 3.529[f] (.065) | 18.68[e] (1.56) 0.71[f] (.05) | 3.763[e] (.293) 3.099[f] (.355) |
| 889 | W | 2.501 (.017) | 2.287 (.001) | 2.182 (.012) | 5.431 (.099) | 27.11 (.45) | 3.824 (.052) | 2.873[e,g] (.314) 3.449[f,g] (.031) | 22.31[e,g] (2.45) 0.673[f,g] (.039) | 2.770[e,g] (.839) 2.657[f,g] (1.029) |
| 896 | W/ Al2024 | 2.550 (.020) | 2.349 (.002) | 2.543 (.022) | 5.286 (.040) | 31.57[j] (.31) | 4.526[j] (.054) | | (VISAR) | |
| 252 | Al1101 | 5.182 (.003) | 2.288 (.001) | 3.102 (.018) | 6.485 (.109) | 46.02 (.52) | 4.385 (.087) | 3.690[e] (.151) | 31.64[e] (2.72) | 3.966[e] (.371) |
| 258 | Ta | 5.041 (.007) | 2.273 (.003) | 4.065 (.020) | 8.133 (.110) | 75.16 (.92) | 4.545 (.072) | 4.949[e] (.208) | 53.07[e] (4.04) | 3.915[e] (.456) |
| 250 | Ta | 5.976 (.003) | 2.324 (.001) | 4.741 (.007) | 9.158 (.055) | 100.90 (.52) | 4.819 (.036) | 5.533[e] (.101) | 64.85[e] (2.10) | 4.446[e] (.147) |
| 262 | Ta | 6.077 (.009) | 2.326 (.003) | 4.803 (.011) | 9.413 (.067) | 105.17 (.66) | 4.750 (.042) | 5.533[e] (.159) 7.505[f] (.228) | 64.84[e] (3.38) 3.57[f] (.38) | 4.470[e] (.191) 3.482[f] (.253) |
| 256 | Ta | 7.058 (.005) | 2.280 (.003) | 5.570 (.028) | 10.228 (.035) | 129.90 (.76) | 5.007 (.039) | | | |

[a] Elastic wave; [b] plastic wave; [c] in laboratory rest frame; [d] free surface; [e] Lexan buffer; [f] polystyrene foam buffer; [g] release data not shown in figures due to large uncertainties; [h] from modelling VISAR data; [i] determined by impedance match—modelling VISAR data gave slightly different results; [j] not shown in figures.

take the pressure of this elastic shock to be the Hugoniot elastic limit of the rhyolite, $P_{HEL} = 2.76 \pm 0.34$ GPa. The velocity of this wave is significantly higher than the zero-pressure ultrasonic *P*-wave velocity, $V_P$, of our samples. It should also be noted that some experiments with slightly lower plastic shock wave velocities had no detectable elastic precursor, indicating that the strength of the rhyolite varies significantly from sample to sample.

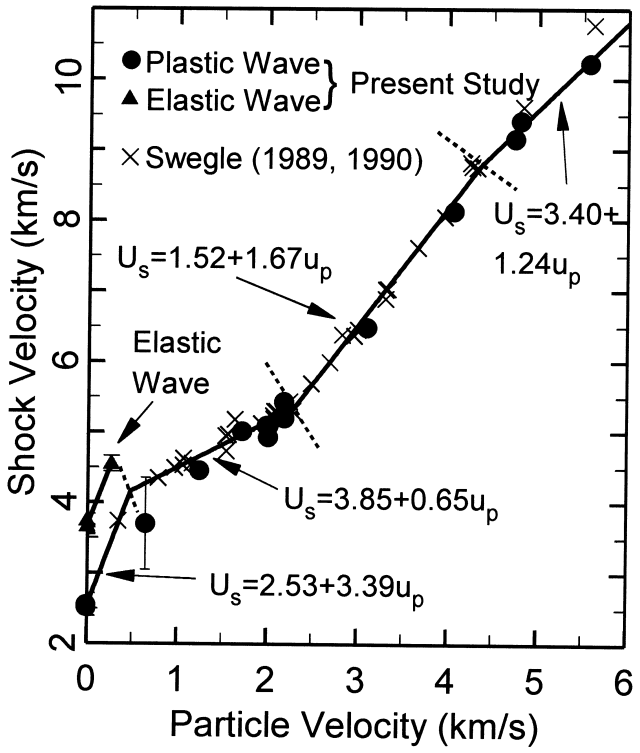


**Figure 2.** Combined shock velocity–particle velocity Hugoniot data set for rhyolite studied by Swegle (1989, 1990) and Kearsage rhyolite. The plotted curve comprises linear segment fits to the combined data set. Dotted lines across the curve separate different linear regions of the Hugoniot.

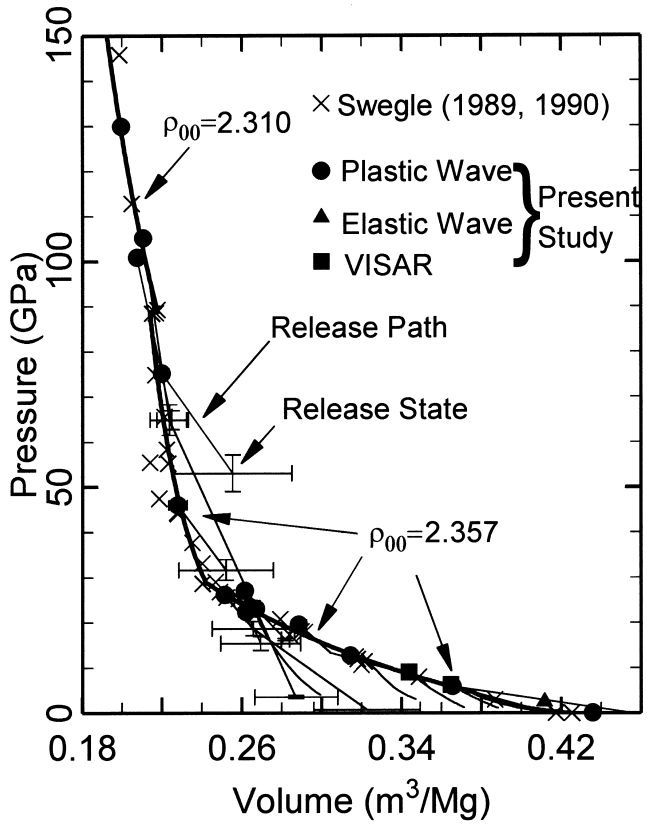


**Figure 3.** Pressure–volume Hugoniot and release adiabat data for rhyolite. The line is the pressure–volume projection of the fitted Hugoniot shown in Fig. 2. The highest pressure portion of the Hugoniot is fitted to data for which the mean initial sample density is $\rho_{00} = 2.310$ Mg m$^{-3}$, whereas the other portions of the curve are for samples with mean initial density of $\rho_{00} = 2.357$ Mg m$^{-3}$. This results in a small discontinuity in the curve at 88 GPa.

## PHASE CHANGES AND EQUATIONS OF STATE

### Fit equations of state

An important use of shock wave equation of state data is to develop equations of state for calculation of properties at conditions away from the Hugoniot or for extrapolation of the Hugoniot to conditions not attainable in conventional experiments. True equations of state refer to single phases, whereas rocks such as rhyolite consist of a mixture of different mineral phases. However, we can obtain an effective equation of state for any situation where none of the constituent phases is in the process of transforming to another phase. Thus, when we speak of a given 'phase', we are referring to a situation in which none of the constituent minerals is undergoing a phase transition. Between single phase regions of the Hugoniot, there are transition regions, made up of a mixture of the lower and higher pressure phases. We can define a fraction $f_{\mathrm{HPP}}$ of the higher pressure phase in the material. At shock pressures below this 'mixed phase' region, the fraction $f_{\mathrm{HPP}}$ of the higher pressure phase is zero. Above the transition region, $f_{\mathrm{HPP}} = 1$. In the mixed phase region, $0 < f_{\mathrm{HPP}} < 1$.

Regions where the slope is very shallow on the $U_s$–$u_p$ and $P$–$V$ Hugoniot curves often correspond to phase transitions characterized by a large volume decrease. The combined data set shows clear evidence of two such transition regions. The first extends from ~10 to ~40 GPa. In this pressure range, most of the minerals making up rhyolite (including quartz and feldspars) transform to solid high-pressure polymorphs. We treat the original, low-pressure mineral assemblage as a single low-pressure phase (LPP) and the equivalent assemblage of high-pressure polymorphs as the rhyolite high-pressure phase (HPP). The intervening transition region is a mixed-phase region consisting of a mixture of LPP and HPP. The second transition region begins at ~90 GPa, with an upper limit that is at present poorly defined by the data but estimated to be at ~120 GPa. Based on the similarity between the qualitative behaviour of the rhyolite and quartz Hugoniot curves and the fact that crystal-density $SiO_2$ melts on the Hugoniot at about 110 GPa (Lyzenga *et al.* 1983), we suggest that this region of the Hugoniot represents melting of the HPP to a dense liquid characterized by Si and Al in high (~sixfold) coordination with oxygen.

For the present study, we obtain parameters describing the principal isentropes of the LPP and HPP, with a tentative assignment of parameters to the hypothesized dense liquid, using the third-order Birch–Murnaghan Eulerian finite strain EOS:

$$P_{\mathrm{S}} = \frac{3}{2} K_{0\mathrm{S}} (x^7 - x^5)(1 + \xi - \xi x^2), \qquad (5)$$

**Table 5.** Summary of measured and calculated properties of rhyolite.

| Experimental $U_s$-$u_p$ Hugoniot Curves | | | | | |
|---|---|---|---|---|---|
| Caltech Data | | | Caltech and Swegle Data | | |
| $C_0$ (km/s) | $s$ | $u_p$ range (km/s) | $C_0$ (km/s) | $s$ | $u_p$ range (km/s) |
| 2.99±0.37 | 1.18±0.27 | 0-1.51 | 2.53±0.08 | 3.39±0.37 | 0-0.48 |
| 3.77±0.50 | 0.66±0.24 | 1.51-2.44 | 3.85±0.05 | 0.65±0.03 | 0.48-2.29 |
| 1.32±0.31 | 1.67±0.07 | 2.44-4.75 | 1.52±0.08 | 1.67±0.02 | 2.29-4.37 |
| 3.49±0.36 | 1.21±0.07 | ≥4.75 | 3.40±0.34 | 1.24±0.06 | ≥4.37 |

| Calculated $U_s$-$u_p$ Hugoniot Curves | | | | |
|---|---|---|---|---|
| | $C_0$ (km/s) | $s$ | $s'$ (s/km) | $u_p$ range (km/s) |
| Calculated from fit EOS parameters | 1.24 | 6.58 | -3.15 | 0-0.79 |
| | 4.19 | 0.304 | 0.107 | 0.79-2.60 |
| | 0.55 | 2.107 | -0.046 | 2.60-4.35 |
| | 1.68 | 1.995 | -0.08 | 4.35-5.16 |
| | 1.89 | 1.45 | -0.0178 | ≥5.16 |
| Water Saturated, Calculated from EOS | 3.14 | 3.29 | -1.27 | 0-0.67 |
| | 4.63 | 0.153 | 0.112 | 0.67-2.48 |
| | 0.79 | 2.105 | -0.504 | 2.48-4.24 |
| | 2.13 | 1.97 | -0.0933 | 4.24-5.10 |
| | 1.82 | 1.514 | 0.0081 | ≥5.10 |

| Fit Equation of State Parameters | | | | | | |
|---|---|---|---|---|---|---|
| Phase | $\rho_0$ (Mg/m$^3$) | $K_{S0}$ (GPa) | $K'$ | $\gamma_0$ | $n$ | $E_{tr}$ (MJ/kg) |
| Low $P$ Solid | 2.494±.002 | 37±2 | 6.27±.25 | 1 | 1 | 0 |
| High $P$ Solid | 3.848±.080 | 128±20 | 3.7±1.4 | 1.5±0.5 | 0±0.5 | 0.7±0.1 |
| High $P$ Liquid | 3.71±.10 | 127±25 | 2.1±1.0 | 1.5±1.0 | 0±1 | 2.0±0.5 |

$$E_S = -\int_{V_0}^{V_H} P_S\, dV$$
$$= \frac{9}{2} V_0 K_{0S}\left[\frac{x^4}{4} - \frac{x^2}{2} + \frac{1}{4} - \xi\left(\frac{x^6}{6} - \frac{x^4}{4} + \frac{x^2}{2} - \frac{1}{6}\right)\right], \quad (6)$$

where

$$x = \left(\frac{V_0}{V_H}\right)^{1/3} \quad (7)$$

and

$$\xi = \frac{3}{4}(4 - K'). \quad (8)$$

$P_S$ is the pressure on the isentrope and $E_S$ is the internal energy gained on compression along the isentrope from $V_0$ to $V_H$. For conditions away from the isentrope, we use the Mie–Grüneisen EOS, with the assumption that the Grüneisen parameter $\gamma \equiv V(\partial P/\partial E)_V$ obeys

$$\gamma = \gamma_0\left(\frac{V}{V_0}\right)^n. \quad (9)$$

The Hugoniot curve is calculated by equating the energy gained by following two thermodynamic paths to the final shock state and can be expressed as

$$P_H = \frac{E_S + E_{tr} - \frac{V_H}{\gamma_H} P_S}{\frac{V_{00} - V_H}{2} - \frac{V_H}{\gamma_H}}, \quad (10)$$

where $E_{tr}$ is the energy required to transform the sample from its initial phase to the Hugoniot phase at ambient conditions. The subscript 'H' refers to the value on the Hugoniot.

The LPP behaviour of the rhyolite is complicated by several factors. First is the fact that the material exhibits finite strength. Second, rhyolite is a mixture of materials with different properties. If we take the corrected normative mineral assemblage in Table 3, including the water not chemically bound (i.e. adsorbed water, shown as $H_2O^-$ in Table 2), and calculate the density of this assemblage without porosity, we obtain a density of $2.494 \pm 0.002$ Mg m$^{-3}$, very close to the mean measured Archimedian density of $2.4929 \pm 0.0005$ Mg m$^{-3}$. Given this agreement, we take the value of $\rho_0$ for the low-pressure phase as $2.494 \pm 0.002$ Mg m$^{-3}$. The agreement between the calculated non-porous density and the Archimedian density suggests that the porosity in the rock is well-connected.

Although we could try to average the zero-pressure properties of the component minerals to obtain EOS parameters for the low-pressure phase, the resulting average gives large high-order derivatives of $K_S$ because the rock is composed of a mixture of phases with very different elastic properties. We chose instead to model the Hugoniot curve by assuming the Hugoniot volume of the rhyolite to be a mass-weighted average of the volumes of the individual constituents on their respective Hugoniot curves at the same pressure:

$$V_H = \sum_i m_i V_{H,i}, \tag{11}$$

where $V_{H,i}$ and $m_i$ are the specific volume and mass fraction, respectively, of mineral $i$ at the same pressure on its respective Hugoniot for the same porosity. This approach gives an estimated Hugoniot curve that is fit by $K_{S0} = 37 \pm 2$ GPa and $K' = 6.27 \pm 0.25$ under the assumption that $\gamma_0 = 1$ and $n = 1$. These values of $K_{S0}$ and $K'$ are not the true zero-pressure properties of the low-pressure phase, as is evident from the measured ultrasonic wave velocities, but give a good estimate of the effective EOS in the shock pressure range in which this phase exists.

Unlike the low-pressure phase discussed above, we cannot predict EOS parameters for the HPP of rhyolite because the properties of the individual mineral high-pressure phases are not yet sufficiently constrained, especially when we attempt to account for the presence of $H_2O$ in the rock. Instead, we fit the EOS parameters to the experimental data, using the mineral parameters only to provide supplementary information on quantities not well constrained by the data.

Part of the problem in obtaining an accurate EOS is choosing the range of data so as to avoid mixed-phase regions. For the HPP, we use data in the pressure range from 40 to 90 GPa. The energy of transition, $E_{tr}$, is insensitive to the fit, so we chose the mass-weighted average of values for the constituent minerals (Table 6), which gives $E_{tr} = 0.7 \pm 0.1$ MJ kg$^{-1}$. The remainder of the parameters were allowed to vary in the fitting process. Obtaining a satisfactory fit was complicated by the presence of outliers in the data. Two points from Swegle (1989) were excluded from the fit because they fall well off the trend established by the remainder of the data. The fit was further complicated by near-singularity resulting from the steepness of the $P$–$V$ Hugoniot, so that the solution was conducted by iterative improvement of the fit. The final fit, which was further constrained to have parameters which are consistent with the composition of the rock, gives $\rho_0 = 3.834 \pm 0.080$ Mg m$^{-3}$, $K_{S0} = 128 \pm 20$ GPa, $K' = 3.7 \pm 1.4$, $\gamma_0 = 1.5 \pm 0.5$ and $n = 0.0 \pm 0.5$. It should be emphasized that the large uncertainties on the fit parameters are a result of a high degree of correlation between the different parameters and do not imply a poor fit to the data. Even with the large uncertainties, the values presented here are significantly different from those used by Swegle (1989, 1990),

**Table 6.** Mineral equation of state parameters used for mixture modelling.

| Mineral (Phase) | $\rho_0$ (Mg/m$^3$) | $K_{S0}$ (GPa) | $K'$ | $\gamma_0$ | $n$ | $E_{tr}$ (MJ/kg) | Reference |
|---|---|---|---|---|---|---|---|
| Quartz (LPP) | 2.650 | 37.7 | 6.4 | 0.7 | 2.0 | --- | 1 |
| Quartz (HPP) | 4.2901 | 306 | 5.4 | 1.38 | 3.2 | 0.82 | 2 |
| Orthoclase (LPP) | 2.5601 | 54 | 4.4 | 1.0 | 1.0 | --- | 3, 11 |
| Orthoclase (HPP) | 3.840 | 236 | 2.3 | 1.0 | 1.0 | 1.03 | 4 |
| Albite (LPP) | 2.611 | 70 | 4.0 | 1.0 | 1.0 | --- | 5, 6, 11, 12 |
| Anorthite (LPP) | 2.7603 | 94 | 4.0 | 1.0 | 1.0 | --- | 5, 6, 11, 12 |
| Albite-rich Plagioclase (HPP) | 3.700 | 186 | 2.6 | 1.0 | 1.0 | 0.46 | 4 |
| Muscovite | 2.835 | 52 | 3.2 | 0.72 | 1.0 | --- | 7 |
| Hypersthene (LPP) | 3.300 | 106 | 9.6 | 1.6 | 1.5 | --- | 8 |
| Hypersthene (HPP) | 4.277 | 262 | 4.0 | 2.0 | 1.5 | 1.60 | 8, 12 |
| Magnetite (LPP) | 5.194 | 181.9 | 4.0 | 1.0 | 1.0 | --- | 9, 11, 12 |
| Magnetite (HPP) | 6.5 | 195 | 3.4 | 1.8 | 1.0 | 0.42 | 9, 10 |

1. Swegle (1989, 199).
2. Lyzenga *et al.* (1983).
3. Ahrens & Liu (1973).
4. Sekine & Ahrens (1992).
5. Angel *et al.* (1988).
6. Robie *et al.* (1978).
7. Sekine *et al.* (1991).
8. Watt & Ahrens (1986).
9. Syono *et al.* (1977).
10. No published EOS. We assumed HPP $K_{S0}$, $K'$, $\gamma_0$, $n$, and $E_{tr}$ are the same as for the FeO HPP (Jeanloz & Ahrens 1980).
11. Assumed $\gamma_0 = 1$ and $n = 1$.
12. $K' = 4$ assumed.

who explicitly assumed that rhyolite HPP EOS parameters would be similar to those of pure $SiO_2$. However, the values we obtain are expected to be much closer to those that would be obtained if estimates were made based on the mineral composition of rhyolite. In particular, the value of $\rho_0$ we obtain is very close to that of a mixture of the high-pressure phase of quartz (stishovite) (Lyzenga *et al.* 1983) and feldspars (Sekine & Ahrens 1992) in the proportions given in the modified norm.

In addition to the formation of a high-pressure phase that is complete at $P \approx 40$ GPa, the data also suggest a second major phase transition that begins in the 90–100 GPa pressure range. Based on the similarity between the rhyolite and $SiO_2$ Hugoniot curves and the observation of melting on the quartz Hugoniot at $\sim 100$ GPa (Lyzenga *et al.* 1983), we suggest that the rhyolite HPP is undergoing melting to a liquid with a high coordination number (CN). The data above 90 GPa are insufficient to reliably delineate the boundary between the HPP–liquid mixed-phase region and the liquid single-phase region of the Hugoniot, so we cannot obtain an independent estimate of the values of EOS parameters for the dense liquid. We can, however, make an estimate of the liquid EOS by assuming that the ratios between HPP and liquid EOS parameters (i.e. $K_{S0}$, etc.) are the same for $SiO_2$ and rhyolite. We have made this assumption for $\rho_0$, $K_{S0}$ and $E_{tr}$. We also assumed that $\gamma_0 = 1.5$ and $n = 0$. We then chose the value of $K'$ most consistent with the two highest pressure data. The provisional equation of state we obtain for the liquid is given by the parameters listed in Table 5.

### Mixed-phase regions

The mixed-phase (MP) regions between the single-phase portions of the Hugoniot are complicated by the fact that they contain varying proportions of two separate phases. We can model the MP regions of the Hugoniot using the Watt & Ahrens (1984) model:

$$V_H = f_2 V_{H,2} + (1 - f_2) V_{H,1}, \quad (12)$$

$$E_H = f_2 E_{H,2} + (1 - f_2) E_{H,1}, \quad (13)$$

where subscripts '1' and '2' denote the lower- and higher-pressure phases on the Hugoniot, respectively. The quantity $f_2$ is the fraction of the higher-pressure phase in the mixture. We explicitly assume here that only two phases will coexist in a given MP region. $V_H$ and $E_H$ for both the high- and low-pressure phases are calculated for a shock with the initial conditions of the Hugoniot we wish to model. The task thus becomes one of calculating $f_2$.

How to calculate the value of $f_2$ is problematic. If the system were able to maintain thermodynamic equilibrium, then the ratio of the two phases would be controlled by (and buffer) the $P$–$T$ conditions of the shock state through minimization of the Gibbs free energy while obeying conservation of energy. The transition seems to be kinetically inhibited, as it is for quartz (Zhugin 1996). The mechanisms responsible for the observed transition rates are not yet understood. As a result, we must rely on empirical data to determine how the ratios of phases vary in the transition regions for an initial starting condition.

In the absence of a suitable physical model of the phase transition kinetics, we use the simple assumption that $f_2$ varies linearly with pressure within the mixed-phase regions. Fig. 4 shows the values of the fractions of each phase used, as a function of shock pressure. The Hugoniot that results when these values of $f_2$ are used with the equations of state listed in Table 5 is compared with the data in Figs 5 and 6. The $U_s$–$u_p$ projection of the Hugoniot consists of five curvilinear segments, rather than the four linear segments originally identified from the data. These segments can be described by quadratic $U_s$–$u_p$ relations using the parameters given in Table 5.

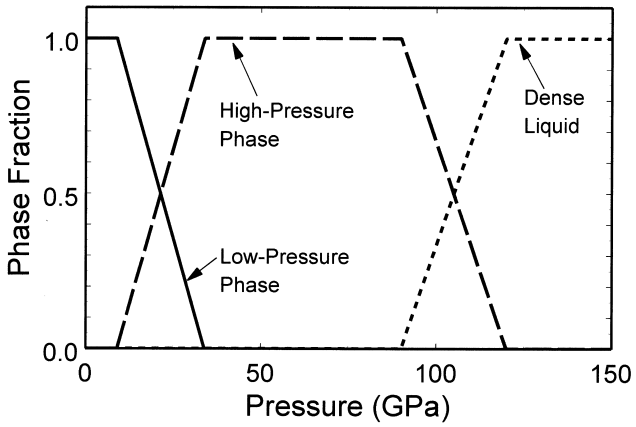


**Figure 4.** Mass fraction of low-pressure solid phase, high-pressure solid phase and dense liquid phase assumed in calculating the Hugoniot from fitted equations of state via eqs (12)–(13).

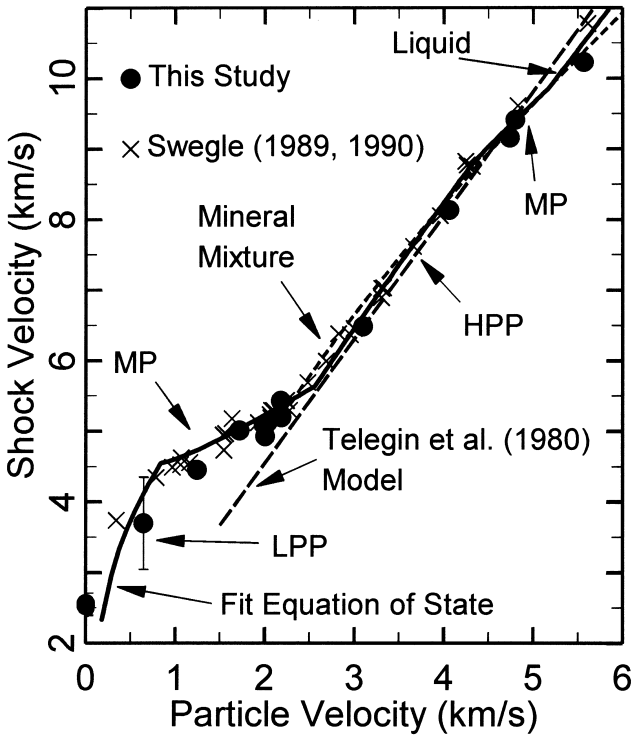


**Figure 5.** Shock velocity–particle velocity experimental data compared with calculated Hugoniot from the fitted equations of state and phase mixing models, compared with the Telegin *et al.* (1980) oxide mixing model and the Al'tshuler & Sharipdzhanov (1971) mineral mixture model. The labels LPP, MP and HPP refer to the low-pressure phase, mixed-phase and high-pressure phase regions of the Hugoniot, respectively.

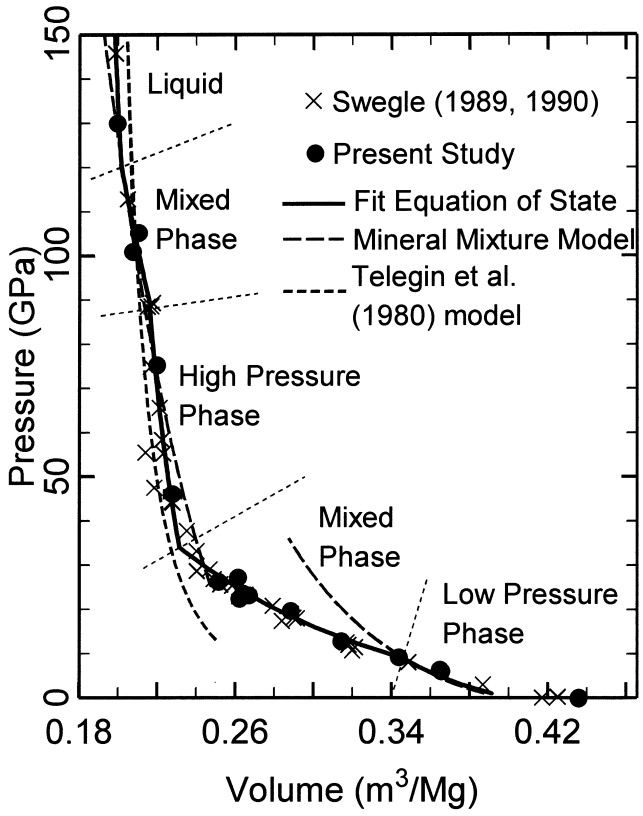


**Figure 6.** Pressure–volume Hugoniot data compared with calculated Hugoniots from equations of state and phase-mixing models and from the mineral mixture model of Al'tshuler & Sharipdzhanov (1971) and the oxide mixing model of Telegin *et al.* (1980). The dotted lines across the solid curve delineate the boundaries of the single-phase regions of the Hugoniot.

### Composition-based EOS estimates

Although the shock wave data allow the direct estimation of EOS parameters, we also wish to test the validity of models which might be used to calculate the effects of changes in composition of the shock wave behaviour of a given rock. We consider two models for the prediction of the Hugoniot, based on the composition of the rhyolite. The first is the oxide mixing model of Telegin *et al.* (1980), who demonstrated good agreement between experimental data and a model which gives $C_0$ and $s$ in the HPP region as a function of the oxide composition and density of the rock. According to their model,

$$C_0 = a_0 + a_1\rho_{00} + \sum_i a_i z_i, \tag{14}$$

$$s = b_0 + b_1\rho_{00} + \sum_i b_i z_i, \tag{15}$$

where $z_i$ is the weight percentage of component $i$ and $a_0$, $a_1$, $a_i$, $b_0$, $b_1$, and $b_i$ are constants. Using the constants given by Telegin *et al.* (1980), we get $C_0 = 1.039$ km s$^{-1}$ and $s = 1.755$ for $\rho_{00} = 2.3651$ Mg m$^{-3}$. This line is plotted in Fig. 5. As can be seen, this model is successful at describing the Hugoniot at higher velocities, but cannot reproduce the effects of phase transitions.

We also model the Hugoniot using the mixing model of Al'tshuler & Sharipdzhanov (1971), using the Hugoniot curves of the constituent minerals in the corrected CIPW norm with the relation given in eq. (11). The mineral LPP and HPP (when appropriate) Hugoniots were calculated for an initial porosity of 5.5 per cent from published equations of state. For calculation of the mineral Hugoniot curves, we use the EOS parameters listed in Table 6 with the Birch–Murnaghan and Mie–Grüneisen equations of state. The water Hugoniot is calculated from the experimental $U_s$–$u_p$ relation given by $C_0 = 1.497$ km s$^{-1}$ and $s = 1.875$ for $u_p \leq 1.653$ km s$^{-1}$ [based on a fit to the data presented by Marsh (1980)] and $C_0 = 2.393$ km s$^{-1}$ and $s = 1.333$ for $u_p > 1.653$ km s$^{-1}$ (Mitchell & Nellis 1982) and corrected for porosity using the EOS model developed for water by Bakanova *et al.* (1976). Fig. 6 presents results for both the LPP and HPP regions. The HPP portion of the mineral mixture Hugoniot, while not following the data in detail, does provide a fairly good approximation of the overall data set above the LPP–HPP mixed-phase region. The deviation in the LPP portion of the Hugoniot is readily explained by the fact that the rhyolite still exhibits strength, as evidenced by the presence of an elastic wave preceding the deformational shock in some cases. This results in incomplete crushing of the pores in the rock, resulting in a larger volume than is predicted by the model.

### Heat capacity and temperature

Lyzenga *et al.* (1983) observe that measured temperatures in shocked $SiO_2$ overshoot the phase boundary for melting of the $SiO_2$ HPP. This overshoot is presumably due to kinetic inhibition of the transition, although such an overshoot is also observed in KBr and CsBr (Boness & Brown 1993), which as ionic compounds should be less subject to kinetic effects than covalent solids like $SiO_2$. The transition region in the $SiO_2$ data, as inferred from shock temperature measurements, is much narrower than that inferred for rhyolite, suggesting that the phase transition in rhyolite is closer to equilibrium. As a result, we expect the temperature overshoot to be much smaller, if it occurs at all. We can estimate the shock temperature in phase $i$ of rhyolite via

$$T_{H,i} = T_{S,i} + \frac{V_{H,i}}{\gamma_{H,i} C_{V,i}}(P_H - P_{S,i}), \tag{16}$$

$$T_{S,i} = T_0 \exp\left( - \int_{V_{0,i}}^{V_{H,i}} \frac{\gamma_i}{V} dV \right). \tag{17}$$

While we do not have any data on the high-pressure specific heat, we assume that the liquidus of a rhyolitic composition should be no higher than that of pure $SiO_2$. Using this to set a lower limit on $C_V$, we adopt the value $C_V = 2147$ J kg$^{-1}$ K$^{-1}$ which is a factor of 1.6 higher than the Dulong–Petit limit of $3R$. Lyzenga *et al.* (1983) also found that the required value of $C_V$ was significantly higher than $3R$ for $SiO_2$. We use the same value of $C_V$ for all three single phases. In the MP regions, the assumption that $C_V$ is equal for all phases allows the Hugoniot temperature to be calculated in the same way as energy and volume in the mixed phase regions. The resulting $P$–$T$ curve is shown in Fig. 7. The calculated values of $T_H$ suggest that there will be no overshoot, as expected. We also show the phase boundaries in the $SiO_2$ system (Ahrens 1996)

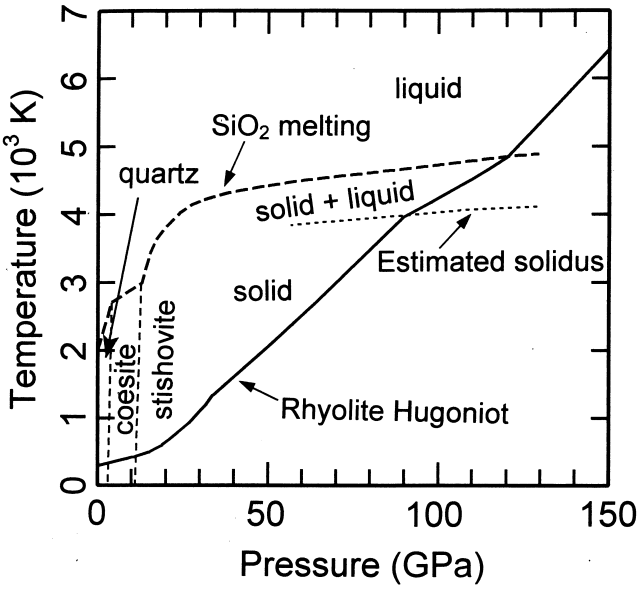


**Figure 7.** Calculated Hugoniot temperatures as a function of shock pressure in 5.5 per cent porous rhyolite with a specific heat of 4.8*R*. Also shown are phase boundaries for $SiO_2$ from Ahrens (1996) and a portion of the estimated solidus for a rhyolitic composition.

and a suggested solidus for a rhyolitic composition, based on the positions of the phase boundaries in the data.

## RELEASE ISENTROPES AND ENERGY DEPOSITION

Volumes of the impedance matching release points were obtained via the Riemann integral formula (Lyzenga & Ahrens 1978):

$$u_r = u_p + \int_{P_r}^{P_H} \left( -\left(\frac{\partial V}{\partial P}\right)_{ad} \right)^{1/2} dP, \tag{18}$$

where the subscript 'r' refers to the release state and the subscript 'ad' denotes the path along the release adiabat. Unfortunately, the release path is not in general known *a priori*. Formally minimized volumes may be obtained if the release path is assumed to be a straight line in the *P*–*V* plane. While this slightly underestimates the true release state volume, a better estimate requires *a priori* knowledge of the equation of state of the Hugoniot phase. Thus, using the straight-line approximation is best for the present case in that it gives a rigorous lower bound on the release state volume. In cases where two different release states were obtained from two different buffers or a buffer and an inclined mirror, the value of $u_r$ for the lower pressure release point is obtained by replacing $P_H$ in eq. (18) with the value of $P_r$ from the first release point and $u_p$ with the value of $u_r$ from the first release point, thus giving a piecewise linear release path. The resulting values are given in Table 4 and shown in Fig. 8. Also shown in Figs 3 and 8 are the release paths calculated by modelling the VISAR data.

If we make the assumption that $C_V$ is constant, then the pressure on the release adiabat in the absence of phase transitions during release can be calculated analytically. Well above the Debye temperature, the assumption of constant $C_V$ is rigorously correct. For situations where the temperature is

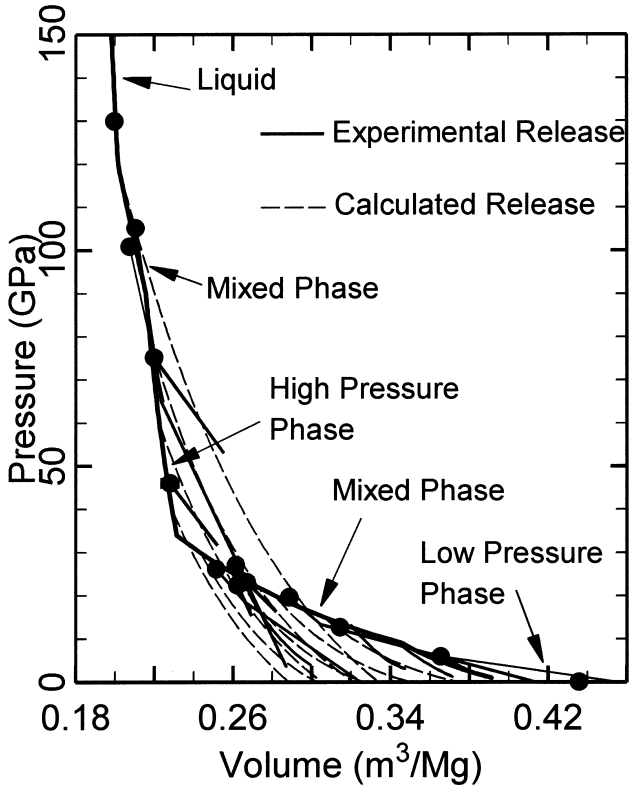


**Figure 8.** Experimental release adiabats compared with calculated release curves based on fitted equations of state, assuming no reversion to lower pressure phases during release. Experimental release paths are centred on the experimental Hugoniot data.

lower than the Debye temperature, the equations we present will not be rigorously correct, but the errors are unlikely to be worse than those introduced by uncertainties in the values of EOS parameters used in our model. Because the single-phase release adiabat is an isentrope, all points on the release path, including the Hugoniot state to which the release path is anchored, are at the same entropy *S*. This also requires that all points on the release path will have the same entropy $\Delta S$ relative to the principal isentrope described by the EOS parameters via eqs (5)–(8). At the Hugoniot volume $V_H$, this is

$$\Delta S = \int_{T_S}^{T_H} \frac{C_V}{T}\, dT = C_V \ln\left(\frac{T_H}{T_S}\right), \tag{19}$$

where $T_H$ and $T_S$ are the temperatures on the Hugoniot and the principal isentrope, respectively. If we expand this by using the expressions for $T_H$ and $T_S$ in eqs (16) and (17), we get

$$\Delta S = C_V \ln\left\{ \frac{(P_H - P_S)V_H/\gamma_H}{T_0 \exp\left[ -\int_{V_0}^{V_H} (\gamma/V)\, dV \right]} + 1 \right\} \tag{20}$$

Now let us choose a volume $V_r$ characterizing a point on the release path. The constant entropy condition requires that the

release state pressure must obey

$$C_V \ln\left\{\frac{(P_r - P_{S,r})V_r/\gamma_r}{T_0 \exp\left[-\int_{V_o}^{V_r}(\gamma/V)\,dV\right]} + 1\right\}$$

$$= C_V \ln\left\{\frac{(P_H - P_S)V_H/\gamma_H}{T_0 \exp\left[-\int_{V_o}^{V_H}(\gamma/V)\,dV\right]} + 1\right\}, \quad (21)$$

where the subscript 'r' refers to the value calculated at $V_r$. By inspection, we can see that this expression requires

$$(P_r - P_{S,r})\frac{V_r}{\gamma_r} = (P_H - P_S)\frac{V_H}{\gamma_H}\exp\left(\int_{V_o}^{V_H}\frac{\gamma}{V}\,dV - \int_{V_o}^{V_r}\frac{\gamma}{V}\,dV\right). \quad (22)$$

Noting that we assume $\gamma$ obeys eq. (9), this is rearranged to give $P_r$:

$$P_r = P_{S,r} + (P_H - P_S)(V_H/V_r)^{n-1}\exp\left(\int_{V_r}^{V_H}\frac{\gamma}{V}\,dV\right). \quad (23)$$

The internal energy of the release state, relative to the initial internal energy before the shock compression process, is

$$E_r = E_{S,r} + E_{tr} + \frac{V_r}{\gamma_r}(P_r - P_{S,r}). \quad (24)$$

Release adiabats originating in the LPP portion of the Hugoniot are completely described by the above equations all the way to $P = 0$. For higher pressure phases and the mixed-phase portions of the Hugoniot, however, the behaviour may be more complicated. The kinetic inhibitions that affect phase changes during shock compression can also affect reversion to lower-pressure phases upon release. Sekine *et al.* (1995) model release adiabats from the HPP portion of the Hugoniot of granite by assuming that reversion to LPP is inhibited and the HPP is thus 'frozen in' down to some critical pressure $P_c$, with formation of diaplectic glass upon further release. The present data give no indication of diaplectic glass formation or of reversion to lower-pressure phases. This is true for both the high-pressure solid and liquid phases. Since the rock contains hydrous phases, we expect $H_2O$ gas to be evolved as $P$ approaches zero, but have ignored that effect in the present discussion.

Fig. 8 shows the release adiabats predicted by our model, in comparison with the data, demonstrating the good agreement between the calculated and experimental release adiabats. One consequence of having a successful model for the shock and release behaviour of rhyolite is that we can also determine the amount of energy irreversibly deposited in the rock during the shock and release process. This energy is manifested as latent heat of transformation from the initial phase to the final, post-shock, phase, with the remainder of the excess energy being sensible heat. We call the fraction of $E_H$ that is irreversibly deposited $f'$. It is given by

$$f' = \frac{E_H - E_r}{E_H}. \quad (25)$$

Fig. 9 gives the estimates for $f'$ as a function of Hugoniot pressure $P_H$.

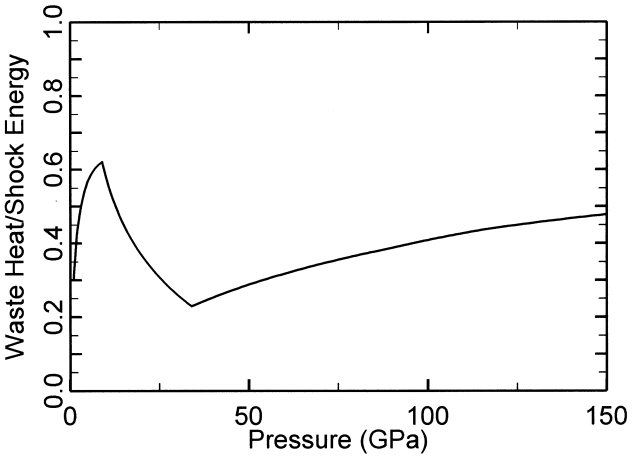


**Figure 9.** Fraction of Rankine–Hugoniot (shock) internal energy irreversibly deposited (waste heat) in 5.5 per cent porous dry Kearsage rhyolite by the passage of shock wave and subsequent adiabatic release to zero pressure.

## HUGONIOT OF SATURATED RHYOLITE

The Hugoniot of a saturated rock can be accurately calculated by using the mixing model of Al'tshuler & Sharipdzhanov (1971) but taking the saturated rock as a mixture of dry, non-porous rock with water in the correct proportions. Kearsage rhyolite with 5.5 per cent porosity, corresponding to the average dry density of our samples and those studied by Swegle (1989), results in a mass fraction of pore-filling water of 0.0212 when the rock is saturated. It must be pointed out that this is only the water required to fill the pores in the dry rock; the water determined in the chemical analysis of the rock is considered to be part of the dry rock. The calculated density of fully saturated 5.5 per cent porous Kearsage rhyolite is 2.412 Mg m$^{-3}$. Since the shock wave moves faster than the characteristic elastic wave speed of the rock, the details of pore structure are generally unimportant to the shock propagation behaviour. The primary effect of a pore-filling fluid such as water is to mitigate pore collapse, shifting the Hugoniot curve to somewhat higher volumes (and thus also higher shock wave velocities) at low pressures than for the dry porous rock. This effect is seen for the present case in Figs 10 and 11. At high pressures, however, the effect is mitigated and eventually reversed, apparently because the increased value of $E_H$ in eq. (3), resulting from the lower initial density of the dry rock, includes a sufficient amount of sensible heat to drive the thermal pressure above that of the saturated rock at the same value of $V_H$. As noted earlier for the dry rhyolite, the LPP region is complicated by the presence of an elastic precursor, so that the LPP Hugoniot parameters cannot be used reliably. They are most useful for calculation of states in the MP region via the volume conservation mixing model of Watt & Ahrens (1984). Parameters for the quadratic $U_s$–$u_p$ relations corresponding to this model for saturated rhyolite are given in Table 5.

We can also apply the oxide mixing model of Telegin *et al.* (1980) to the experimental $U_s$–$u_p$ Hugoniot. This is accomplished by modifying the experimentally determined values of $C_0$ and $s$ as follows:

$$C_{0,sat} = (C_{0,exp} - a_0 - a_1\rho_{00,exp})(1 - m_{H_2O}) + a_0 + a_1\rho_{0,sat} + 100 m_{H_2O} a_{H_2O}, \quad (26)$$

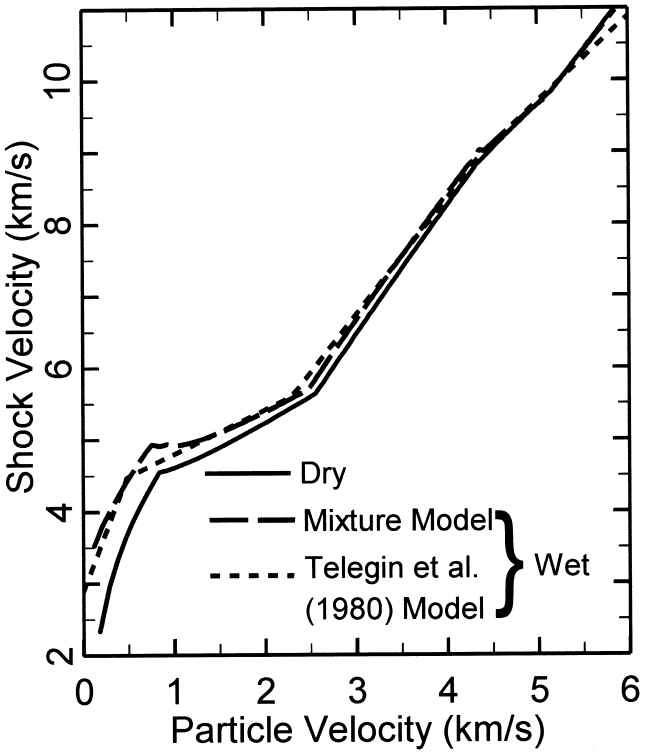


**Figure 10.** Effects of water saturation on the pressure–volume Hugoniot of 5.5 per cent porous Kearsage rhyolite. The saturated rock Hugoniot is calculated by modelling as a mixture of water and non-porous rock in appropriate proportions via eq. (11).

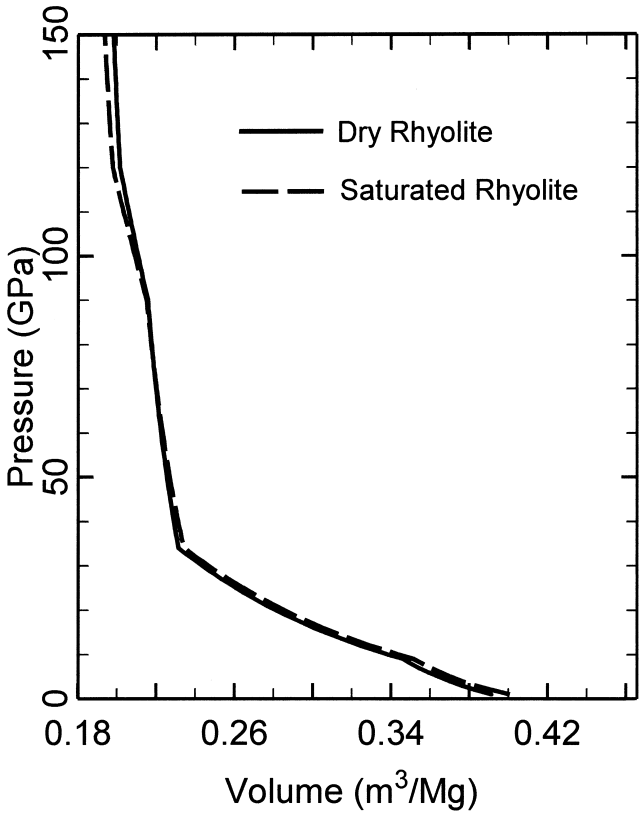


**Figure 11.** Effect of water saturation on shock velocity–particle velocity Hugoniot of 5.5 per cent porous Kearsage rhyolite. The mixture model used the equation of state parameters for Kearsage rhyolite given in Table 5. The experimental shock velocity–particle velocity Hugoniot is used as a basis for describing the rock component of the mixture for use with the Telegin *et al.* (1980) model.

$$s_{0,\mathrm{sat}} = (s_{0,\mathrm{exp}} - b_0 - b_1\rho_{00,\mathrm{exp}})(1 - m_{\mathrm{H_2O}}) + b_0 + b_1\rho_{0,\mathrm{sat}} + 100 m_{\mathrm{H_2O}} b_{\mathrm{H_2O}}\,, \quad (27)$$

where $m_{\mathrm{H_2O}}$ is the mass fraction of pore-filling water. The factor of 100 in the last term of both equations is used with the published values of $a_{\mathrm{H_2O}}$ and $b_{\mathrm{H_2O}}$ from Telegin *et al.* (1980) because these published values are stated for the mass percentage rather than the mass fraction. The resulting Hugoniot, shown in Fig. 11, is described by $C_0 = 2.89$ km s$^{-1}$ and $s = 3.30$ for $u_p < 0.48$ km s$^{-1}$; $C_0 = 4.18$ km s$^{-1}$ and $s = 0.62$ for 0.48 km s$^{-1} \le u_p < 2.29$ km s$^{-1}$; $C_0 = 1.90$ km s$^{-1}$ and $s = 1.61$ for 2.29 km s$^{-1} \le u_p < 4.38$ km s$^{-1}$; and $C_0 = 3.74$ km s$^{-1}$ and $s = 1.19$ for $u_p \ge 4.38$ km s$^{-1}$.

Since the elastic precursor at low particle velocities is dependent upon the properties of the rock surrounding the pores and does not depend upon the pores, the presence of a fluid filling the pores should have little effect on the speed of the elastic precursor. The calculated value of $P_{\mathrm{el}}$ will, of course, increase slightly because of the slightly greater density of the saturated rock. The pressure at which the elastic wave is overdriven may decrease, however, because mitigation of pore collapse by the fluid decreases the effective compressibility of the rock, with an attendant increase in the plastic wave velocity.

For release from the shocked state, we can use the same model for the water-saturated rock as for the dry rock with the same values of $K_{S0}$ and $K'$. However, the higher specific volumes of the shock and release states for the saturated case require that the LPP release be modelled by the saturated LPP $P$–$V$ Hugoniot and that the value of $P_c$ be changed. Also, we expect that release from the HPP and possibly the MP regimes will result in the water converting to the gas phase once the material drops below the $H_2O$ critical pressure of 0.022 GPa.

## CONCLUSION

We have obtained new shock wave equation of state and release adiabat data for rhyolite. These data are combined with those of Swegle (1989, 1990) to give an experimental Hugoniot which is described by eq. (4) with the fit parameters given in Table 5. We suggest that the Hugoniot data give evidence of three distinct phases: both low- and high-pressure solid phases and a dense, high coordination number liquid. Equation of state parameters for these phases, along with parameters calculated for dry and water-saturated Hugoniot curves, are summarized in Table 5. Mixed-phase portions of the Hugoniot are modelled by mass-weighted averages of the volumes of the end-member Hugoniot states. The fraction of a given end-member phase is assumed to vary linearly with pressure within the mixed-phase region. These regions cover the ranges of 9–34 GPa for the low-pressure–high-pressure solid mixed-phase region, and 90–120 GPa for the high-pressure solid–liquid mixed-phase region. The equation of state parameters for the three phases accurately describe both shock and release states.

Comparisons of these equations of state with the release adiabat data suggest that the high-pressure phases do not revert to either a lower pressure phase or a diaplectic glass upon release. Combination of the shock and release paths allows us to estimate that 20–60 per cent of the Hugoniot energy is retained as waste heat in the rock upon release.

Water-saturated rhyolite will have a similar Hugoniot to the dry rock. The primary effect of a pore-filling fluid such as water is to decrease the effective compressibility by mitigating pore collapse. At lower shock pressures, this has the expected result of increasing the volume of the Hugoniot state. At high pressures, the effect is reversed as a result of the decreased internal energy of the shock state, which leads to smaller thermal pressures at a given volume, thus shifting the Hugoniot below that of porous rock. The Hugoniot may be estimated using the method suggested by Al'tshuler & Sharipdzhanov (1971), using the dry, non-porous rock and water as the components of a binary mixture.

## ACKNOWLEDGMENTS

We thank E. Gelle and M. Long for assistance in the experiments and R. Blandford, R. Stagat, S. Peyton and K. McLaughlin for helpful technical discussions. This work was supported by NASA Grant NAGW-1941 and by the US Air Force Technical Applications Center under subcontract #SC-0064-90-0002 from Mission Research Corporation. Contribution 5634, Division of Geological and Planetary Sciences.

## REFERENCES

Ahrens, T.J., 1987. Shock wave techniques for geophysics and planetary physics, in *Methods of Experimental Physics,* 24, pp. 185–235, eds Sammis, C.G. & Henyey, T.L., Academic Press, San Diego.

Ahrens, T.J., 1996. Applications of shock compression science to earth and planetary physics, in *Shock Compression of Condensed Matter—1995,* pp. 3–8, eds Schmidt, S.C. & Tao, W.C., AIP Press, Woodbury, NY.

Ahrens, T.J. & Liu, H.-P., 1973. A shock-induced phase change in orthoclase, *J. geophys. Res.,* **78,** 1274–1278.

Al'tshuler, L.V. & Sharipdzhanov, I.I., 1971. Additive equations of state of silicates at high pressures, *Izv. Earth Physics,* 167–177 (English transl.).

Angel, R.J., Hazen, R.M., McCormick, T.C., Prewitt, C.T. & Smyth, J.R., 1988. Comparative compressibility of end-member feldspars, *Phys. Chem. Minerals,* **15,** 313–318.

Bakanova, A.A., Zubarev, V.N., Sutalov, Y.N. & Trunin, R.F., 1976. Thermodynamic properties of water at high pressures and temperatures, *Sov. Phys. JETP,* **41,** 544–548 (English transl.).

Barker, L.M. & Hollenbach, R.E., 1972. Laser interferometer for measuring high velocities of any reflecting surface, *J. appl. Phys.,* **43,** 4669–4675.

Boness, D.A. & Brown, J.M., 1993. Bulk superheating of solid KBr and CsBr with shock waves, *Phys. Rev. Lett.,* **71,** 2931–2934.

Hemsing, W., 1979. Velocity sensing interferometry (VISAR) modification, *Rev. Sci. Instrum.,* **50,** 73–78.

Jeanloz, R. & Ahrens, T.J., 1980. Equations of state of FeO and CaO, *Geophys. J. R. astr. Soc.,* **62,** 505–528.

Kelsey, C.H., 1965. Calculation of the C.I.P.W. norm, *Mineral. Mag.,* 276–282.

Kipp, M.E. & Lawrence, R.J., 1982. WONDY V—A One-dimensional Finite Difference Propagation Code, *Sandia National Laboratories Report SAND 81-0930.*

Lyzenga, G.A. & Ahrens, T.J., 1978. The relation between the shock-induced free-surface velocity and the postshock specific volume of solids, *J. appl. Phys.,* **49,** 201–204.

Lyzenga, G.A., Ahrens, T.J. & Mitchell, A.C., 1983. Shock temperatures of $SiO_2$ and their implications, *J. geophys. Res.,* **88,** 2431–2444.

Marsh, S.P., 1980. *LASL Shock Hugoniot Data,* University of California Press, Los Angeles.

Mitchell, A.C. & Nellis, W.J., 1982. Equation of state and electrical conductivity of water and ammonia shocked to the 100 GPa (1 Mbar) pressure range, *J. chem. Phys.,* **76,** 6273–6281.

Rice, M.H., McQueen, R.G. & Walsh, J.M., 1958. Compression of solids by strong shock waves, *Solid State Phys.,* **6,** 1–63.

Robie, R.A., Hemingway, B.S. & Fisher, J.R., 1978. *Thermodynamic Properties of Mineral and Related Substances at 298.15 K and 1 Bar ($10^5$ Pascals) Pressure and at Higher Temperatures,* USGS Bull. 1452.

Sekine, T. & Ahrens, T.J., 1992. Shock-induced transformations in the system $NaAlSiO_4$-$SiO_2$: a new interpretation, *Phys. Chem. Miner.,* **18,** 359–364.

Sekine, T., Duffy, T.S., Rubin, A.M., Anderson, W.W. & Ahrens, T.J., 1995. Shock compression and isentropic release of granite, *Geophys. J. Int.,* **120,** 247–261.

Sekine, T., Rubin, A.M. & Ahrens, T.J., 1991. Shock wave equation of state of muscovite, *J. geophys. Res.,* **96,** 19 675–19 680.

Swegle, J.W., 1989. Irreversible Phase Transitions and Wave Propagation in Silicate Geologic Materials, *Sandia National Laboratories, Report SAND 89-1443.*

Swegle, J.W., 1990. Irreversible phase transitions and wave propagation in silicate geologic materials, *J. appl. Phys.,* **68,** 1563–1579.

Syono, Y., Goto, T. & Nakagawa, Y., 1977. Phase-transition pressures of $Fe_3O_4$ and GaAs determined from shock-compression experiments, in *High Pressure Research: Application in Geophysics,* pp. 463–476, eds Manghnani, M.H. & Akimoto, S., Academic Press, New York.

Telegin, G.S., Antoshev, V.G., Bugayeva, V.A., Simakov, G.V. & Trunin, R.F., 1980. Calculated determination of Hugoniot curves of rocks and minerals, *Izv. Earth Physics,* **16,** 319–324 (English transl.).

Trunin, R.F., Simakov, G.V., Dudoladev, I.P., Telegin, G.S. & Trusov, I.P., 1988. Rock compressibility in shock waves, *Izv. Earth Physics,* **24,** 38–42 (English transl.).

Watt, J.P. & Ahrens, T.J., 1984. Shock wave equations of state using mixed-phase regime data, *J. geophys. Res.,* **89,** 7836–7844.

Watt, J.P. & Ahrens, T.J., 1986. Shock wave equation of state of enstatite, *J. geophys. Res.,* **91,** 7495–7503.

Yang, W., Chen, G., Anderson, W.W. & Ahrens, T.J., 1994. Shock compression and isentropic release of rhyolite, in *High-Pressure Science and Technology, 1993,* pp. 1115–1118, eds Schmidt, S.C., Shaner, J.W., Samara, G.A. & Ross, M., American Institute of Physics, New York.

Zhugin, Yu.N., 1996. The behavior of α-quartz under high dynamic and static pressures: new results and views, in *Shock Compression of Condensed Matter—1995,* pp. 97–100, eds Schmidt, C. & Tao, W.C., AIP Press, Woodbury, NY.